SCIENTIFIC REPORTS

OPEN

SUBJECT AREAS:
PHASE TRANSITIONS AND CRITICAL PHENOMENA
SUPERCONDUCTING PROPERTIES AND MATERIALS

Received
13 March 2014

Accepted
19 August 2014

Published
22 September 2014

Correspondence and requests for materials should be addressed to J.S. (jiansun@nju.edu.cn) or Z.X. (zwxing@nju.edu.cn)

Novel structural phases and superconductivity of iridium telluride under high pressures

Bin Li[1,2,5], Guiqin Huang[2,3], Jian Sun[2,5] & Zhongwen Xing[4,5]

[1]College of Science, Nanjing University of Posts and Telecommunications, Nanjing 210023, China, [2]National Laboratory of Solid State Microstructures and School of Physics, Nanjing University, Nanjing 210093, China, [3]Department of Physics, Nanjing Normal University, Nanjing 210023, China, [4]Department of Materials Science and Engineering, Nanjing University, Nanjing 210093, China, [5]Collaborative Innovation Center of Advanced Microstructures, Nanjing University, Nanjing 210093, China.

Transition metal selenide and telluride have recently receive considerable attention due to their possible structural relation to ferropnictide. Pressure is often used as an efficient way to modify the crystal or electronic structure that in many cases lead to new material states of interest. Here we search the structures of $IrTe_2$ up to 150 GPa using crystal structure prediction techniques combining with *ab initio* calculations. Three new stable phases under high pressures are predicted, and their electronic structure properties, phonon spectra, and electron-phonon couplings are also investigated. Significant reconstructions of band structures and Fermi surfaces are found in these new phases. Calculated results show that while the C2/m-2 phase has bad metal behavior and very weak electron-phonon coupling, the $Pa\bar{3}$ and I4/mmm phases have relatively higher electron-phonon coupling up to ~ 1.5 and 0.7, respectively. The variable-composition searching have been performed, newly compounds with different stoichiometries, such as $IrTe_3$, IrTe, and Ir_3Te, are predicted to be thermodynamically and dynamically stable at high pressures. The pressure range investigated here is accessible in the diamond anvil cell experiments, thus our results might stimulate further experimental studies.

In recent years, 5*d* transitional metal iridium ditelluride ($IrTe_2$) has attracted much interest due to its peculiar structural/electronic phase transitions and emergence of superconductivity upon chemical doping or intercalation[1–8]. It was reported[9] that $IrTe_2$ undergoes a structural phase transition at about 250 K from a high-temperature trigonal ($P\bar{3}m1$) to a low-temperaure monoclinic ($C2/m$) structure, accompanied by temperature-dependent anomalies of electron resistivity and magnetic susceptibility. $IrTe_2$ exhibits superconductivity when the structural phase transition is suppressed by chemical doping or intercalation[1–3]. Since the structural phase transition is characterized by the formation and breaking of Ir-Ir bonds along the *b*-axis, the superconductivity can be interpreted by bond-breaking-induced superconductivity[1,10]. On the other hand, it has been proposed to understand this phase transition down to the electron-structure level. Yang *et al.*[2] suggested that the phase transition is a charge-orbital density wave type, and superconductivity up to 3 K sets in as soon as the density wave transition is suppressed by Pd intercalation and substitution. Ootsuki *et al.*[3] argued that the orbitally induced Peierls effect plays an important role in the charge-orbital instability and superconductivity of $Ir_{1-x}Pt_xTe_2$. Recent optical spectroscopic measurements and density functional theory calculations indicated that the transition is not driven by the density wave type instability but caused by the crystal field effect which further splits/separates the energy levels of Te (p_x and p_y) and Te (p_z) bands[6]. A local bonding instability associated with the Te 5p states was suggested as a main factor dominating the structure and the superconductivity[7,8].

It is well known that pressure can efficiently modify the atomic and electronic structures of materials, leading to the formation of novel materials with unusual physical properties, and crystal structure can play a crucial role in the appearance of superconductivity. Recently, a pressure-induced superconductivity was reported in $AuTe_2$ and its bulk superconductivity appears only in the high-pressure phase[10]. Therefore, it is highly desirable to search for new structural phases of $IrTe_2$ under high pressures and investigate the origin of possible superconductivity.

In this work, we use crystal structural prediction techniques to find energetically stable/metastable structures of $IrTe_2$ under high pressures up to 150 GPa. Several novel crystal structures for $IrTe_2$ are predicted in different pressure regions, i.e., the $Pa\bar{3}$ one with 4 formula units (f.u.)/cell, the $C2/m$-2 one with 2 f.u./cell, and the $I4/mmm$ one with 1 f.u./cell. The electronic structure, phonon spectrum, and electron-phonon (EP) coupling are

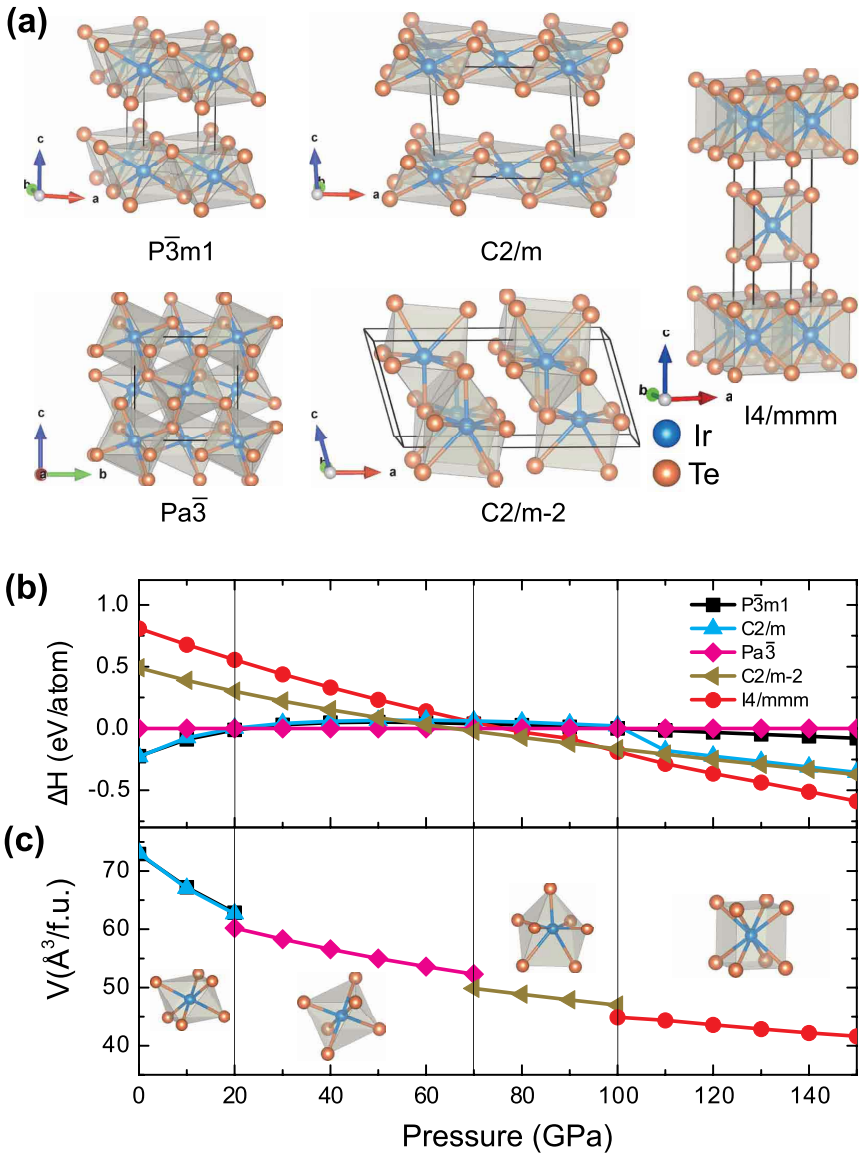

Figure 1 | Crystal structure and equation of states of the $IrTe_2$ phases. (a) Five types of crystallographic structures of $IrTe_2$, and (b) enthalpy relative to that of the $Pa\bar{3}$ phase vs pressure and (c) volume vs pressure curves for various structures. Insets in (c) show different type of polyhedron formed under pressure.

investigated for each phase. The calculated results show that the band structures and Fermi surfaces (FSs) for the high-pressure phases have dramatically reconstructed. It is found that the $Pa\bar{3}$ and $I4/mmm$ phases have relatively strong electron-phonon coupling, which will be of benefit to possible superconductivity. We also have carried out the variable-composition search. Newly found compounds such as $IrTe_3$, IrTe, and Ir_3Te are thermodynamically and dynamically stable and have unusual electronic and phonon properties.

Results and Discussion

Structural and Bonding analysis. First, we use crystal structural prediction techniques to find energetically stable structures of $IrTe_2$ under high pressures. Five types of crystallographic structures shown in Fig. 1(a) are found to be the stable/metastable phases with lower energies. The calculated enthalpy-pressure (ΔH-P) and volume-pressure (V-P) curves are plotted in Figs. 1(b) and (c) for the structures interested. From Fig. 1(b), we find that with increasing pressure, $IrTe_2$ undergoes a series of structural phase transitions, from the $C2/m$ to $Pa\bar{3}$ structure at about 20 GPa, then to the $C2/m$-2 structure at about 70 GPa, and finally to the $I4/mmm$ structure at about 100 GPa. The $C2/m$ structure consists of two formula units, containing edge-sharing Ir-Te_6 octahedra. Although we did not get any clue in advance and "predict" the $Pa\bar{3}$ phase from scratch, this structure actually has been synthesized in experiment[11], and our theoretical transition pressure to it agree very well with the experimental value. It has a cubic lattice embodying vertex-sharing Ir-Te_6 octahedra. An Ir ion locates at the center of the lattice and other Ir ions lie in the middle of the lattice edges. The $C2/m$-2 structure has the same symmetry as the $C2/m$ one, but it exhibits a two-dimensional (2D) characteristic in the xz plane. The Ir and Te ions form an unique edge-sharing Ir-Te_7 octahedron in the lattice. For the $I4/mmm$ structure, each Ir ion is surrounded by eight Te ions, forming an Ir-Te_8 cuboid, and it consists of a stack of Ir-Te_8 cuboid arranging along the z direction. It's interesting that upon pressure, the coordination number of Ir ions increases continuously, forming a series of atomic polyhedrons of Ir-Te_6 → Ir-Te_7 → Ir-Te_8. From Fig. 1(c), one sees that there is a sudden drop in volume at each critical pressure, indicating a first-order structural phase transition there. The optimized structural parameters for these five $IrTe_2$ phases discussed above are listed in Table I.

Table I | Optimized structural parameters of five structures for $IrTe_2$ calculated with PBE and DFT-D2 methods. The parameters of $C2/m$ and $C2/m$-2 shown here correspond to the primitive cell. Note that the volumes are unified in one formula unit

	$P\bar{3}m1$		$C2/m$		$Pa\bar{3}$		$C2/m$-2		$I4/mmm$	
	PBE	DFT-D2	PBE	DFT-D2	PBE	DFT-D2	PBE	DFT-D2	PBE	DFT-D2
P (GPa)	0		0		40		80		120	
a (Å)	3.9512	3.9034	3.9640	3.9115	6.0938	6.0437	5.7235	5.6862	2.8896	2.8394
b (Å)	3.9512	3.9034	3.9640	3.9115	6.0938	6.0437	5.7235	5.6862	2.8896	2.8394
c (Å)	5.3943	5.2713	5.4544	5.2885	6.0938	6.0437	5.1286	5.0852	10.4389	10.4848
V (Å^3/f.u.)	72.93	69.55	73.09	69.60	56.57	55.19	48.81	47.80	43.58	42.26
d_{Te-Te}(Å)	3.4781	3.3295	3.4266	3.3201	3.7349	3.3352	3.3764	3.3630	2.8420	2.8557
d_{Te-Ir}(Å)	2.6685	2.6585	2.6655	2.6569	2.5116	2.4920	2.4796	2.4621	2.6088	2.5149
			2.6681	2.6589			2.4814	2.4709		
							2.5306	2.5186		
							2.8015	2.7619		
							2.8950	2.8905		
$N(E_F)$ (states/eV)	1.94	1.90	1.86	2.02	7.05	6.30	1.09	0.87	1.33	1.32

As found in many other system, such as CO[12] and CO_2[13], some of the $IrTe_2$ phases present a laminar crystal structure, we did additional calculations including van der Waals (vdW) correction proposed by Grimme (DFT-D2)[14]. The obtained structural parameters are listed in Table I. The message is that the volume of unit cell for several structures shrinks due to the vdW corrections. The $C2/m$ and $P\bar{3}m1$ structures under ambient condition have the largest percentage of contraction (about 5.3%) and we find this is mainly from the decreasing of the distance between the adjacent $IrTe_2$ layers. However, the magnitude of contraction decreases with increasing pressure, reflect-

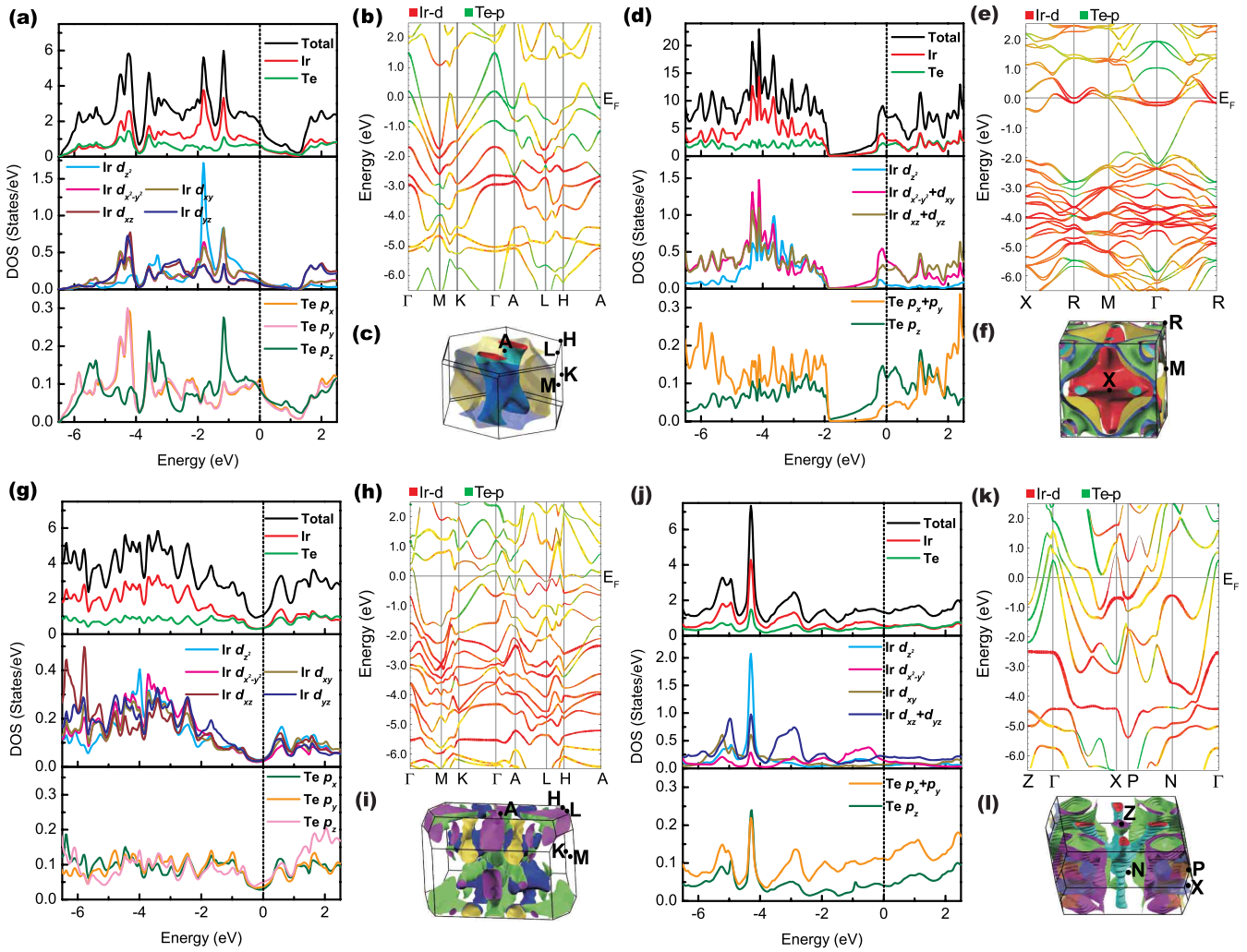

Figure 2 | Electronic structures of the novel $IrTe_2$ phases. Total and partial density of states, fat-band structures with Ir-d and Te-p characteristics, and Fermi surfaces for $C2/m$ at ambient pressure (a) – (c), $Pa\bar{3}$ at 40 GPa (d) – (f), $C2/m$-2 at 80 GPa (g) – (i), and $I4/mmm$ at 120 GPa (j) – (l).

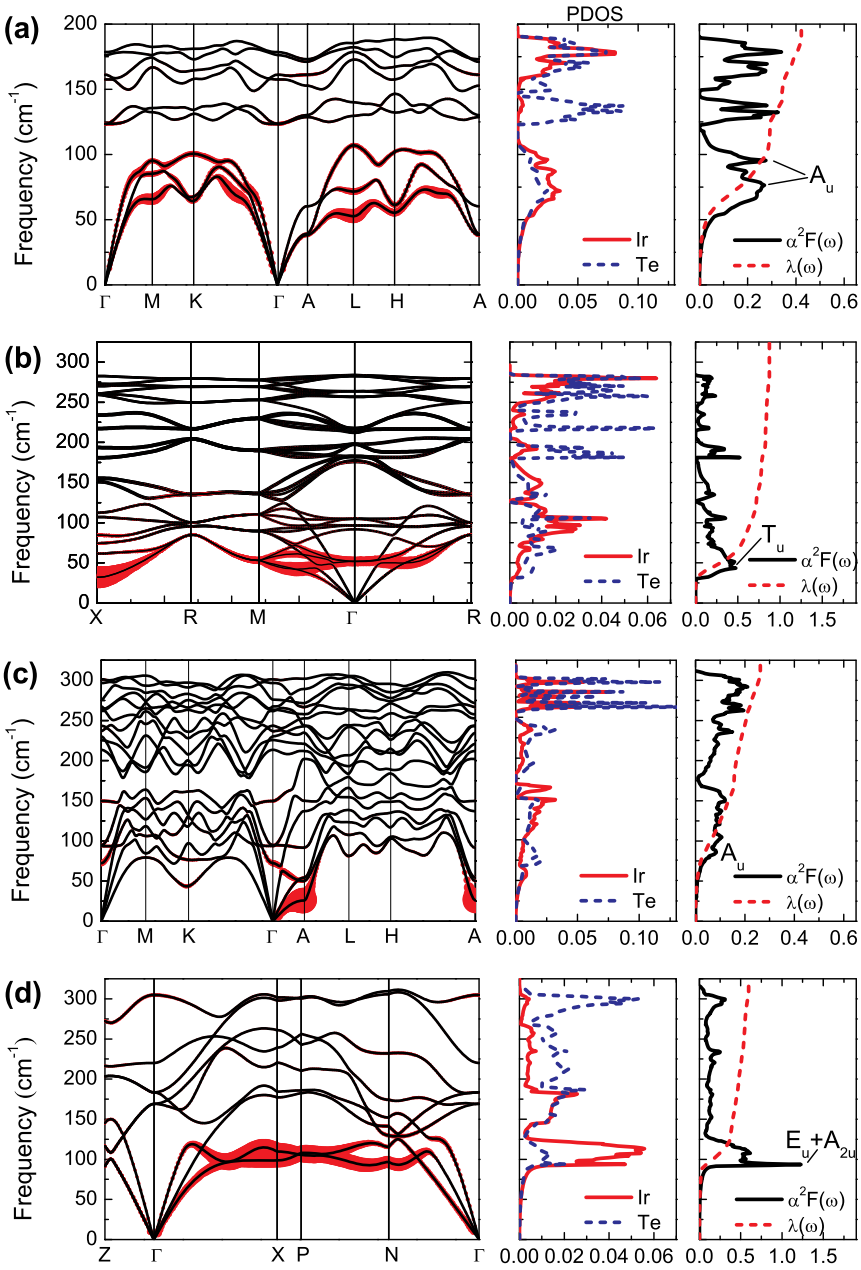

Figure 3 | Calculated phonon dispersions, projected phonon densities of states (PDOS) and Eliashberg spectral function. (from left to right) (a) *C*2/*m* at ambient pressure, (b) $Pa\bar{3}$ at 40 GPa, (c) *C*2/*m*-2 at 80 GPa, and (d) *I*4/*mmm* phases at 120 GPa.

ing that the vdW contribution under high pressure becomes small. Based on the electron localization function (ELF), as showned in the Supporting Informtion, we find there are small overlap between the electrons on the Te atoms in two adjacent layers, both in P$\bar{3}$m1 and C2/m structure, this somehow gives the reason of why the binding energy between the layers are quite large. Without vdW corrections, we obtain the binding energies are 219 meV for P$\bar{3}$m1 and 214 meV for C2/m structure. While with vdW corrections, we obtain 847 meV and 843 meV, respectively.

The calculated total and partial density of states (DOS), band structure with Ir-d and Te-p characteristics, and Fermi surfaces are shown in Fig. 2. For the DOS of the *C*2/*m* structure, the Te p_x orbital exhibits a distinct peak located at the Fermi level (E_F), indicating a small van Hove singularity (vHs) behavior. A recent comprehensive study of the electronic states has revealed the vHs origin of the phase transition between high temperature $P\bar{3}m1$ phase and low temperature *C*2/*m* phase in $IrTe_2$[15]. According to the orbital characteristics of the fat-band, two hybridized Ir 5*d* and Te 5*p* bands cross the Fermi level, forming two Fermi surfaces. Compared with the $P\bar{3}m1$ structure, the interlayer interaction of the *C*2/*m* structure and hence its band dispersion along the *c* axis (Γ-*A* direction) are suppressed, so that the 2D character of the FSs becomes enhanced. The reconfiguration in the topology of FSs along the k_z direction appears to be consistent with what has been observed in angle-resolved photoemission spectroscopy measurements[15–17].

The $Pa\bar{3}$ structure exhibits quite unique electronic structure and Fermi surfaces. There are four bands crossing the Fermi level, which construct four complicated 3D FSs. A van-Hove-like peak lies below the Fermi level 0.1 eV, yielding a large DOS at the Fermi level ($N(E_F)$) ~ 7 states/eV per unit cell, which is contributed mainly by the Ir 5d planar orbitals and the Te p_z orbital. A pseudo gap appears around $E = -1.9$ eV, where a significant Fermi cone originates mainly from the Te *p* orbitals around the Γ point in the band structure. The Fermi level of the *C*2/*m*-2 structure lies at the valley bottom of the DOS

Table 2 | Phonon mode frequencies in units of cm^{-1} at the Γ point for various crystal structure of $IrTe_2$ with I: infrared active and R: Raman active

$P\bar{3}m1$(0 GPa)						
B_u (I)	0	0	154.1	173.4		
A_u (I)	0	173.4				
B_g (R)	115.9					
A_g (R)	116.2	152.9				
$C2/m$ (0 GPa)						
A_u (I)	0	0	0	157.5	176.3	178.6
A_g (R)	123.4	123.6	161.2			
$Pa\bar{3}$(40 GPa)						
T_u (I)	0	51.9	104.9	197.9	263.7	282.6
A_u (I)	91.8	177.8				
E_u (I)	96.7	283.8				
A_g (R)	176.1					
T_g (R)	182.6	217.3	256.8			
E_g (R)	212.5					
$C2/m$-2 (80 GPa)						
A_u (I)	0	0	0	93.7	213.4	230.3
	261.7	263.5	267.5			
A_g (R)	72.3	94.8	149.7	225.7	236.6	243.4
	275.8	296.6	301.3			
$I4/mmm$ (120 GPa)						
A_{2u} (I)	0	220.1				
E_u (I)	0	169.2				
E_g (R)	183.4					
A_{1g} (R)	304.8					

curves and $N(E_F) \sim 1$ states/eV per unit cell, exhibiting a bad metallic behavior. Two bands crossing the Fermi level form the FSs shown in Fig. 2(h). For the $I4/mmm$ structure, the FSs arise from the four bands crossing E_F. Around the Γ point there is a claw-like Fermi pocket with four-fold symmetry, and the Fermi pockets at zone corners are shaped as irregular cylinders. At the same time, there is a reduction of DOS at E_F for $I4/mmm$, $N(E_F) = 1.33$ states/eV, compared with those in the low-pressure phases. The reconstructed band structures and FSs may greatly affect phonon properties and electron-phonon coupling.

Vibrational Analysis. The calculated phonon dispersions, projected phonon densities of states (PDOS), and Eliashberg spectral function $\alpha^2F(\omega)$ are shown from left to right in Fig. 3. In the left panel of Fig. 3, the distribution of the EP coupling for each phonon mode, λ_{qv}, is described by red circles, the radius of the circles being proportional to the magnitude of each λ_{qv}. For the $C2/m$ structure, as shown in Fig. 3(a), the two gaps near 120 cm^{-1} and 150 cm^{-1} in the phonon spectrum divide the spectrum into three regions: the acoustic branches, middle-frequency and high-frequency optical branches. The acoustic modes extend to about 100 cm^{-1}. The modes at the high frequency region are associated with the vibrations of Ir atoms beating against Te atoms. Whereas the modes at the middle frequency region are associate with the vibrations of Te-Te bond stretching. The obtained $\alpha^2F(\omega)$ curve exhibits two main humps below 120 cm^{-1}, which originate from the acoustic A_u modes.

For the $Pa\bar{3}$ structure at 40 GPa [see Fig. 3(b)], phonon frequencies extend up to ~ 280 cm^{-1} and the point group at the Γ point is T_h, which can be decomposed as $\Gamma = A_g \oplus E_g \oplus 3T_g \oplus 2A_u \oplus 2E_u \oplus 6T_u$ with E_g and E_u being double degenerate, and T_g and T_u triple degenerate. There are two tiny gaps in the PDOS, respectively, near 125 cm^{-1} and 210 cm^{-1}. The acoustic phonon modes exhibit a significant phonon softening along all the symmetric directions.

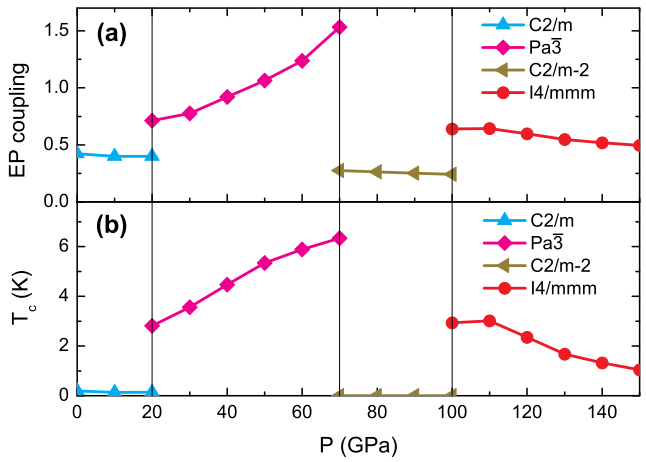

Figure 4 | Calculated superconducting properties of $IrTe_2$ phases as functions of pressure. (a) Calculated electron-phonon coupling and (b) superconducting transition temperature.

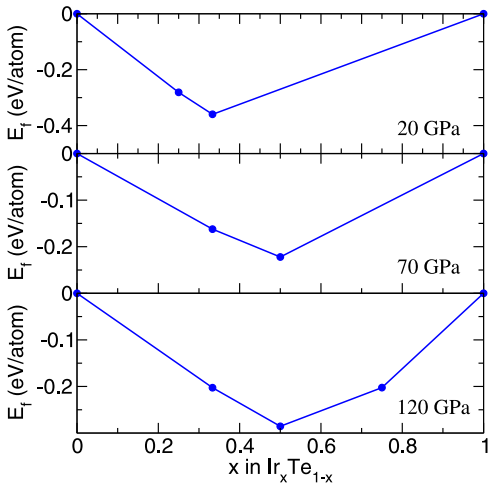

Figure 5 | Formation enthalpies of Ir_xTe_{1-x} per atom with respect to Ir and Te for different Ir-Te phases. The abscissa x is the fraction of Ir in the structures. The blue circles indicate the most stable structures at each stoichiometry.

Table 3 | Optimized structural parameters of $IrTe_3$, IrTe and Ir_3Te, calculated with PBE and DFT-D2 methods

	$IrTe_3$(*R*3*c*)		IrTe(*C*2/*c*)		IrTe(*Cmcm*)		Ir_3Te(*I*4/*mcm*)	
	PBE	DFT-D2	PBE	DFT-D2	PBE	DFT-D2	PBE	DFT-D2
P (GPa)	20		70		120		120	
a (Å)	6.1495	6.0597	5.8466	5.7851	5.0057	4.9743	5.2123	5.1568
b (Å)	6.1495	6.0597	5.8466	5.7851	5.0057	4.9743	5.2123	5.1568
c (Å)	6.1495	6.0597	4.7597	4.7314	4.1410	4.0790	7.4440	7.2929
V (Å^3/f.u.)	85.13	82.33	30.68	29.76	27.57	26.75	50.56	48.48
d_{Te-Te}(Å)	3.3497	3.3144	2.9642	2.9375	2.7679	2.7431	3.6857	3.6464
d_{Te-Ir}(Å)	2.5704	2.5576	2.5161	2.4962	2.5117	2.4895	2.5161	2.5784
	2.5705		2.5599	2.5308	2.5679	2.5382	2.7263	
	2.5707		2.5604	2.5440	2.6833	2.6710		
			2.5773	2.5535				
			2.6947	2.6300				
			2.6979	2.6586				
$N(E_F)$ (states/eV)	2.71	2.32	4.33	4.57	2.73	1.96	5.05	4.84

Furthermore, we notice that the optical branches at the lower frequency side also become soften and merge with the acoustic branches. In the DFPT calculations, the Eliashberg spectral function depends directly on the EP matrix element, $\left|g^{v}_{n\mathbf{k},m(\mathbf{k}+\mathbf{q})}\right|^2$, which is defined as the variation of the self-consistent crystal potential. The low-frequency spectral function curve $\alpha^2F(\omega)$ has two peaks near 50 cm^{-1} and 100 cm^{-1}, which are contributed by the acoustic and optical T_u modes. The latter originate from the out-plane breathing and rocking vibrations of the Ir and Te atoms. The integration of $\lambda(\omega)$ up to 100 cm^{-1} is near 0.7, almost 80% of the total EP coupling. In the $Pa\bar{3}$ phase, the softening of low-frequency modes and enhancement of the Eliashberg spectral function can significantly increase the EP coupling.

For the *C*2/*m*-2 structure at 80 GPa [see Fig. 3(c)], the point group at the Γ point is C_i, same as the *C*2/*m* phase, which can be decomposed as $\Gamma = 9A_u \oplus 9A_g$. Both acoustic and optical branches are hardened and the obtained EP coupling strength is very weak. For the *I*4/*mmm* at 120 GPa [see Fig. 3(d)], the phonon frequencies expand up to more than 300 cm^{-1} and the point group at the Γ point is D_{4h}. The Γ modes can be decomposed as $\Gamma = 2A_{2u} \oplus 2E_u \oplus E_g \oplus A_{1g}$, where E_u and E_g modes are double degenerate. From the PDOS curves, one sees that the low-frequency branches below 125 cm^{-1} are mainly associated with the vibrations of the Ir atoms, whereas the high-frequency branches above 200 cm^{-1} originate mainly from the vibrations of the Te atoms. The $\alpha^2F(\omega)$ curve exhibits a distinct peak around $\omega = 100$ cm^{-1}, and the low-frequency phonons account for more than 60% of the total EP coupling. The calculated phonon vibration frequencies for each $IrTe_2$ compound at the Γ point are listed in Table 2.

Using the Allen-Dynes formula[18,19]

$$T_c = \frac{\omega_{ln}}{1.2}\exp\left[-\frac{1.04(1+\lambda)}{\lambda-\mu^*(1+0.62\lambda)}\right], \quad (1)$$

where ω_{ln} is the logarithmically averaged frequencies, and taking the Coulomb parameter as $\mu^* = 0.15$, we evaluate the pressure-dependent T_c. The obtained λ and T_c as a function of pressure are plotted in Figs. 4 (a) and (b), respectively. It is found that the calculated value is equal to $\lambda \sim 0.4$ for the *C*2/*m* phase and $\lambda \sim 0.25$ for the *C*2/*m*-2 phase. Such weak EP couplings, together with bad metallic behavior in the *C*2/*m*-2 phase, result in almost vanishing T_c. Very interestingly, the predicted value of λ for the $Pa\bar{3}$ phase is enhanced up to $\sim$ 1.5, yielding high-pressure induced superconductivity with $T_c \sim 6$ K. In the *I*4/*mmm* phase, the maximal λ is equal to 0.7 and it decreases with further increasing pressures.

Variable-composition Search. We also investigated the phase stabilities of Ir-Te systems calculating the formation enthalpy of various Ir_xTe_{1-x} compounds, as shown in Fig. 5. The formation enthalpy E_f of Ir_xTe_{1-x} was calculated as

$$E_f(Ir_xTe_{1-x}) = E(Ir_xTe_{1-x}) - xE(Ir) - (1-x)E(Te) \quad (2)$$

In the entire region of explored pressures, $IrTe_2$ stays as a stable compound. The Ir-rich phase emerges at high pressure. Convex hull diagram in Fig. 5 features newly predicted thermodynamically stable compounds: $IrTe_3$ at 20 GPa [Trigonal (space group *R*3*c*)]; IrTe at 70 GPa [Monoclinic (space group *C*2/*c*)] and 120 GPa [Orthorhombic (space group *Cmcm*)]; and Ir_3Te at 120 GPa [Tetragonal (space group *I*4/*mcm*)]. Electronic densities of states show that all of these compounds are good metals. The lattice parameters including the vdW (DFT-D2) correction are shown in Table 3. In $IrTe_3$ and two phases of IrTe, six Te atoms bonding with one Ir atom construct a Ir-Te_6 octahedra. In Ir_3Te, the fundamental unit is consisted by Te-topped cube with Ir atoms locating at the face centers (Fig.S1 in supplementary information). For all the structures, we calculated phonons and EP couplings, and found all of them to be dynamically stable (Fig.S2). The EP couplings given by phonon calculations are from 0.3 to 0.5.

In summary, with crystal structural prediction techniques, it is found that, with increasing pressure, $IrTe_2$ may undergo a series of structural phase transitions: *C*2/*m*→$Pa\bar{3}$→*C*2/*m*-2→*I*4/*mmm*, and the latter three phases under high pressures are newly discovered. For various phases of $IrTe_2$, the electronic band structures, phonon spectra, and electron-phonon couplings have been studied. It is shown that there are relatively higher EP coupling constant in the high-pressure $Pa\bar{3}$ and *I*4/*mmm*. We hope such a pressure induced superconductivity in $IrTe_2$ will stimulate new experiments on this material. The variable-composition search gives unexpected chemical compounds at high pressure with good metal feature. These results suggest that pressure is an effective way to overcome the kinetic barrier to formation in the synthesis of Ir-Te binary system.

Methods

Two crystal structure prediction methods, crystal structure analysis by particle swarm optimization (CALYPSO)[20–22] and *ab initio* random structure searching (AIRSS)[23,24] are employed. Both methods give the same best candidates independently for given chemical compositions and external conditions. The electronic structure calculations with high accuracy for the stable structures are performed using the full-potential linearized augmented plane wave (FP–LAPW) method implemented in the WIEN2K code[25]. The generalized gradient approximation (GGA)[26] is applied to the exchange-correlation potential calculation. The muffin tin radii are chosen to be 2.5 a.u. for Ir and 2.33 a.u. for Te. The plane-wave cutoff is defined by $RK_{max} = 7.0$, where R is the minimum LAPW sphere radius and K_{max} is the plane-wave vector cutoff. The pho-

non calculations are carried out by using a density functional perturbation theory (DFPT) approach through the Quantum-ESPRESSO program[27]. The cutoffs are chosen as 30 Ry for the wave functions and 300 Ry for the charge density. The electronic integration is performed over a $16 \times 16 \times 16$ k-point mesh. Dynamical matrices and the EP couplings are calculated on a $4 \times 4 \times 4$ q-point grid. A dense $24 \times 24 \times 24$ grid is used for evaluating an accurate EP interaction matrix. Due to the large atomic numbers of Ir and Te, the spin-orbit coupling is included in our calculations.

1. Pyon, S., Kudo, K. & Nohara, M. Superconductivity Induced by Bond Breaking in the Triangular Lattice of $IrTe_2$. *J. Phys. Soc. Jpn.* **81**, 053701, DOI:10.1143/JPSJ.81.053701 (2012).
2. Yang, J. J. *et al.* Charge-Orbital Density Wave and Superconductivity in the Strong Spin-Orbit Coupled $IrTe_2$:Pd. *Phys. Rev. Lett.* **108**, 116402, DOI:10.1103/PhysRevLett.108.116402 (2012).
3. Ootsuki, D. *et al.* Orbital degeneracy and Peierls instability in the triangular-lattice superconductor $Ir_{1-x}Pt_xTe_2$. *Phys. Rev. B* **86**, 014519, DOI:10.1103/PhysRevB.86.014519 (2012).
4. Kudo, K., Kobayashi, M., Pyon, S. & Nohara, M. Suppression of Structural Phase Transition in $IrTe_2$ by Isovalent Rh Doping. *J. Phys. Soc. Jpn.* **82**, 085001, DOI:10.7566/JPSJ.82.085001 (2013).
5. Oh, Y. S., Yang, J. J., Horibe, Y. & Cheong, S.-W. Anionic Depolymerization Transition in $IrTe_2$. *Phys. Rev. Lett.* **110** 127209, DOI:10.1103/PhysRevLett.110.127209 (2013).
6. Fang, A. F., Xu, G., Dong, T., Zheng, P. & Wang, N. L. Structural phase transition in $IrTe_2$: A combined study of optical spectroscopy and band structure calculations. *Nature Sci. Rep.* **3**, 1153, DOI:10.1038/srep01153 (2013).
7. Kamitani, M. *et al.* Superconductivity in Cu_xIrTe_2 driven by interlayer hybridization. *Phys. Rev. B* **87**, 180501(R), DOI:10.1103/PhysRevB.87.180501 (2013).
8. Cao, H. *et al.* Origin of the phase transition in $IrTe_2$: Structural modulation and local bonding instability. *Phys. Rev. B* **88**, 115122, DOI:10.1103/PhysRevB.88.115122 (2013).
9. Matsumoto, N., Taniguchi, K., Endoh, R., Takano, H. & Nagata, S. Resistance and Susceptibility Anomalies in $IrTe_2$ and $CuIr_2Te_4$. *J. Low Temp. Phys.* **117**, 1129, DOI:10.1023/A,1022546928480 (1999).
10. Kitagawa, S. *et al.* Pressure-Induced Superconductivity in Mineral Calaverite $AuTe_2$. *J. Phys. Soc. Jpn.* **82** 113704, DOI:10.7566/JPSJ.82.113704 (2013).
11. Léger, J. M., Pereira, A. S., Haines, J., Jobic, S. & Brec, R. Phase transformations of polymeric CdI_2-type $IrTe_2$ under high pressure. *J. Phys. Chem. Solids* **61** 27, DOI: 10.1016/S0022-3697(99)00230-9 (2000).
12. Sun, J., Klug, D. D., Pickard, C. J. & Needs, R. J. Controlling the Bonding and Band Gaps of Solid Carbon Monoxide with Pressure. *Phys. Rev. Lett.* **106** 145502, DOI: 10.1103/Phys-RevLett.106.145502.
13. Sun, J., Klug, D. D., Martoňák, R., Montoya, J. A., Lee, M. S., Scandolo, S. & Tosatti, E. High-pressure polymeric phases of carbon dioxide. *Proc. Nat. Acad. Sci.* **106** 6077, DOI: 10.1073/pnas.0812624106.
14. Grimme, S. Semiempirical GGA-Type Density Functional Constructed with a Long-Range Dispersion Correction. *J. Comput. Chem.* **27** 1787, DOI: 10.1002/jcc.20495 (2006).
15. Qian, T. *et al.* Structural phase transition induced by van Hove singularity in 5*d* transition metal compound $IrTe_2$. *arXiv* : 1311.4946.
16. Ootsuki, D. *et al.* Electronic Structure Reconstruction by Orbital Symmetry Breaking in $IrTe_2$. *J. Phys. Soc. Jpn.* **82** 093704, DOI:10.7566/JPSJ.82.093704 (2013).
17. Ootsuki, D. *et al.* Important Roles of Te 5*p* and Ir 5*d* Spin-Orbit Interactions on the Multi-band Electronic Structure of Triangular Lattice Superconductor $Ir_{1-x}Pt_xTe_2$. *J. Phys. Soc. Jpn.* **83** 033704, DOI:10.7566/JPSJ.83.033704 (2014).
18. Mcmillan, W. Transition Temperature of Strong-Coupled Superconductors. *Phys. Rev.* **167**, 331, DOI:10.1103/PhysRev.167.331 (1968).
19. Allen, P. & Dynes, R. Transition temperature of strong-coupled superconductors reanalyzed. *Phys. Rev. B* **12**, 905, DOI:10.1103/PhysRevB.12.905 (1975).
20. Wang, Y., Lv, J., Zhu, L. & Ma, Y. Crystal structure prediction via particle-swarm optimization. *Phys. Rev. B* **82**, 094116, DOI:10.1103/PhysRevB.82.094116 (2010).
21. Lv, J., Wang, Y., Zhu, L. & Ma, Y. Predicted Novel High-Pressure Phases of Lithium. *Phys. Rev. Lett.* **106**, 015503, DOI:10.1103/PhysRevLett.106.015503 (2011).
22. Wang, Y., Lv, J., Zhu, L. & Ma, Y. CALYPSO: A method for crystal structure prediction. *Comput. Phys. Commun.* **183**, 2063–2070, DOI:10.1016/j.cpc.2012.05.008 (2012).
23. Pickard, C. J. & Needs, R. J. High-Pressure Phases of Silane. *Phys. Rev. Lett.* **97**, 045504, DOI:10.1103/PhysRevLett.97.045504 (2006).
24. Pickard, C. J. & Needs, R. J. *Ab initio* random structure searching. *J. Phys.: Condens. Matter* **23**, 053201, DOI:10.1088/0953-8984/23/5/053201 (2011).
25. Blaha, P., Schwarz, K., Madsen, G. K. H., Kvasnicka, D. & Luitz, J. *WIEN2k, An Augmented Plane Wave + LO Program for Calculating Crystal Properties, TU Wien, Vienna*, (2001).
26. Perdew, J. P., Burke, K. & Ernzerhof, M. Generalized Gradient Approximation Made Simple. *Phys. Rev. Lett.* **77**, 3865, DOI:10.1103/PhysRevLett.77.3865 (1996).
27. Giannozzi, P. *et al.* QUANTUM ESPRESSO: a modular and open-source software project for quantum simulations of materials. *J. Phys.: Condens. Matter* **21**, 395502, DOI:10.1088/0953-8984/21/39/395502 (2009).

Acknowledgments

This work is supported by the State Key Program for Basic Researches of China (2010CB923404, 2014CB921103 and 2015CB921202), the National Natural Science Foundation of China (91021003, 11174125 and 51372112), and the Natural Science Foundation of Jiangsu Province (BK2010012). Part of the calculations were performed on the supercomputer in the High Performance Computing Center (HPCC) of Nanjing University.

Author contributions

B.L. and J.S. performed the calculations, analysed the results and drafted the manuscript. G.H. and Z.X. analysed and discussed the results, and commented the manuscript.

Additional information

Supplementary information accompanies this paper at http://www.nature.com/scientificreports

Competing financial interests: The authors declare no competing financial interests.

How to cite this article: Li, B., Huang, G., Sun, J. & Xing, Z. Novel structural phases and superconductivity of iridium telluride under high pressures. *Sci. Rep.* **4**, 6433; DOI:10.1038/srep06433 (2014).